



1 **Towards an improvement of OSL age uncertainties: modelling OSL ages with systematic errors,**
2 **stratigraphic constraints and radiocarbon ages using the R package 'BayLum'**

3 Guillaume Guérin^{1,2*}, Christelle Lahaye¹, Maryam Heydari¹, Martin Autzen^{3,4}, Jan-Pieter Buylaert^{3,4},
4 Pierre Guibert¹, Mayank Jain³, Sebastian Kreutzer^{5,1}, Andrew S. Murray⁴, Kristina J. Thomsen³, Petra
5 Urbanova¹, Anne Philippe⁶.

6 ¹ UMR 5060 CNRS - Université Bordeaux Montaigne, IRAMAT-CRP2A, Maison de l'archéologie,
7 Esplanade des Antilles, 33607 Pessac cedex, France.

8 ² Univ Rennes, CNRS, Géosciences Rennes, UMR 6118, 35000 Rennes, France

9 ³ Center for Nuclear Technologies, Technical University of Denmark, DTU Risø Campus, DK-4000
10 Roskilde, Denmark.

11 ⁴ Nordic Laboratory for Luminescence Dating, Department of Geoscience, Aarhus University, DTU Risø
12 Campus, DK-4000 Roskilde, Denmark.

13 ⁵Geography & Earth Sciences, Aberystwyth University, Aberystwyth, Wales, United Kingdom

14 ⁶ Jean Leray Laboratory of Mathematics (LMJL), UMR6629 CNRS - Université de Nantes, France.

15

16

17 **Keyword:**

18 OSL dating; Bayesian modelling; R package; Systematic errors; Covariance matrix; Stratigraphic
19 constraints

20 **Abstract**

21 Statistical analysis has become increasingly important in the field of OSL dating since it has become
22 possible to measure signals at the single grain scale. The accuracy of large chronological datasets can
23 benefit from the inclusion, in chronological modelling, of stratigraphic constraints and shared
24 systematic errors. Recently, a number of Bayesian models have been developed for OSL age
25 calculation; the R package 'BayLum' allows implementing different such models, in particular for
26 samples in stratigraphic order which share systematic errors. We first show how to introduce
27 stratigraphic constraints in 'BayLum'; then, we focus on the construction, based on measurement
28 uncertainties, of dose covariance matrices to account for systematic errors specific to OSL dating. The
29 nature (systematic versus random) of errors affecting OSL ages is discussed, based – as an example –
30 on the dose rate determination procedure at the IRAMAT-CRP2A laboratory (Bordeaux). The effects of
31 the stratigraphic constraints and dose covariance matrices are illustrated on example datasets. In
32 particular, the interest of combining the modelling of systematic errors with independent ages,
33 unaffected by these errors, is demonstrated. Finally, we discuss other common ways of estimating
34 dose rates and how they may be taken into account in the covariance matrix by other potential users
35 and laboratories. Test datasets are provided as supplementary material to the reader, together with
36 an R Markdown tutorial allowing to reproduce all calculations and figures presented in this study.

37



38 1. Introduction

39 Optically stimulated luminescence (OSL; Huntley *et al.*, 1985) allows dating the last exposure
40 of quartz grains to sunlight. The Single Aliquot Regenerative (SAR) dose protocol consists of comparing
41 the natural luminescence signal to laboratory-generated signals induced by artificial irradiations
42 (Murray and Wintle, 2000; Wintle and Murray, 2006). The corresponding measurements, in particular
43 at the single-grain scale, result in large datasets characterised by important scatter, owing to a number
44 of dispersion factors (see, *e.g.* Thomsen *et al.*, 2005). An OSL age is then obtained by dividing the
45 equivalent dose (i.e. in the case of coarse quartz grains, the dose absorbed by the mineral) by the dose
46 rate to which quartz grains were exposed since the last exposure to light.

47 Statistical analysis, in the field of geochronology, generally aims at improving the precision,
48 accuracy and/or range of dating methods. In the case of OSL dating, calibration errors on the laboratory
49 source dose rate for natural dose estimation, and geochemical standards for dose rate assessment,
50 have so far resulted in age uncertainties of, at best, ~5% (see, *e.g.*, Duller, 2008; Guérin *et al.*, 2013).

51 Note that in what follows, the unit of analysis is a sediment sample; the system of analysis is
52 the laboratory in which the measurements are performed and includes both the apparatus and
53 associated calibration standards. By definition, an error is the difference between the measured or
54 observed value of a physical quantity, and its true (but unknown) value. Thus, by systematic errors, we
55 refer to random errors affecting equipment calibration: whereas each of these errors may be assigned
56 a Gaussian probability density function with zero mean and a known variance (the square root of the
57 variance being generally referred to as uncertainty), at the scale of the laboratory this error takes a
58 fixed, unknown value that affects all measurements in the same direction.

59 Over the past few years, several models for routine Bayesian analysis of SAR OSL and dose rate
60 data were developed to reflect better, and take advantage of, the measurement procedures
61 implemented to calculate OSL ages. Among those models, Combès *et al.* (2015) proposed one for
62 calculating the central dose values for well-bleached samples, leading to higher overall accuracy (see
63 Guérin *et al.*, 2015a) compared to the most commonly used model for OSL data analysis (the Central
64 Dose Model: CDM, Galbraith *et al.*, 1999; note: we changed the original terminology following
65 Galbraith and Roberts, 2012). Combès and Philippe (2017) developed models capable of dealing with
66 individual and systematic multiplicative errors for OSL age calculation including stratigraphic
67 constraints (for general introductions on a statistical analysis of OSL data, but also the statistical
68 models discussed hereafter and associated prior distributions, the reader is referred to Combès *et al.*,
69 2015; Combès and Philippe, 2017, and references therein).

70 To implement the Bayesian models of Combès *et al.* (2015) and Combès and Philippe (2017) in
71 practice, and provide easy access to the community, an R package (R Core Team, 2020) named
72 'BayLum' (Christophe *et al.*, 2020; version 0.2.0) has been developed and released on the
73 Comprehensive R Archive Network (CRAN; see also Mercier *et al.*, 2017, for a first implementation of
74 the central dose model from Combès *et al.*, 2015). First features of this 'BayLum' package were
75 presented by Philippe *et al.* (2019) and its performances, when one is confronted either with large
76 dose values or with dose variability issues, were tested in laboratory-controlled experiments (Heydari
77 and Guérin, 2018) and later applied to various case studies (Lahaye *et al.*, 2018; Carter *et al.*, 2019;
78 Heydari *et al.*, 2020; submitted; Chevrier *et al.*, accepted).

79 The purpose of this paper is to focus on the treatment of stratigraphic constraints and
80 systematic errors for chronological modelling using 'BayLum', *i.e.* it goes beyond than what was first
81 demonstrated by Philippe *et al.* (2019); together with the association of independent, more precise
82 ages (^{14}C in this work), such modelling is expected to reduce OSL age uncertainties. In the past, other



83 approaches to model systematic and random, individual errors in the field of palaeodosimetric dating
84 methods were proposed; in particular, Millard (2006a, 2006b) developed a Bayesian approach quite
85 close to that presented here, but which – among different other things (see Combès and Philippe,
86 2017, for a more detailed discussion) – is limited in its applicability.

87 Herein we present a Bayesian modelling case study. (1) We start with how data should be pre-
88 treated prior to using the ‘BayLum’ package; a simple example of chronological modelling (samples
89 considered independent, *i.e.* without stratigraphic constraints and shared errors) is first presented,
90 yielding an output from the ‘BayLum’ package to serve as a reference for the following, more elaborate
91 models. (2) In the next step, we detail how the user can integrate stratigraphic constraints and the
92 effect on the chronological inference. (3) Then, most importantly we explain how to build a dose
93 covariance matrix in practice to take into account systematic errors (for the definition of this matrix,
94 the reader is referred to Combès and Philippe, 2017) and what effect it has on a series of ages. (4) For
95 this purpose, we base our approach on dose rate measurements as performed by Guérin *et al.* (2015b)
96 at the IRAMAT-CRP2A laboratory. The effect of integrating independent data such as radiocarbon ages,
97 which do not share the systematic errors affecting OSL data, is then illustrated. (5) Finally, we discuss
98 different ways to measure dose rates and various assumptions that can be made regarding the nature
99 (systematic or random) of additional sources of errors in OSL dating.

100 To help the reader, we provide as supplementary information an R markdown document with
101 commented lines of code and example datasets, so that everything presented here may be
102 reproduced.

103 **2. Samples and methods**

104 **2.1. Case study**

105 To illustrate how to model OSL ages, both in stratigraphic constraints and sharing systematic
106 errors, using the R ‘BayLum’ package, we use the data from two sediment samples (FER 1 and FER 3)
107 already dated by quartz OSL (Guérin *et al.*, 2015b). These samples were taken from the archaeological
108 site of La Ferrassie (France) and prepared following standard chemical preparation procedures applied
109 to luminescence-dating samples. While modelling with ‘BayLum’ may be applied to both multi-grain
110 and single-grain OSL datasets, in the following we only focus on single-grain data, as this is probably
111 where the need for appropriate statistical models is most acute (the reliability of multi-grain OSL has
112 been demonstrated when using a plain average (mean) for palaeodose estimation; see, *e.g.*, Murray
113 and Olley, 2002; for theoretical justification, see Guérin *et al.*, 2017). Single-grain OSL data were
114 measured using an automated Risø TL/OSL reader (DA 20) fitted with a single grain attachment (Duller
115 *et al.*, 1999; Bøtter-Jensen *et al.*, 2000). A standard SAR protocol (Murray and Wintle, 2000; 2003) was
116 used to measure single-grain equivalent doses, after checking its suitability for the samples under
117 investigation. A comparison between quartz OSL and feldspar IRSL signals for these two samples, as
118 well as comparison with radiocarbon, showed that these samples were well-bleached at the time of
119 deposition and unaffected by post-depositional mixing. As a result, the use of central dose models is
120 fully justified (it should be noted here that at the time of writing, ‘BayLum’ does not yet include the
121 Bayesian model of Christophe *et al.*, 2018, allowing the analysis of poorly bleached samples).

122 **2.2. Data pre-treatment**

123 The Bayesian modelling implemented in ‘BayLum’ requires information of different natures: (i)
124 raw OSL data in the form of BIN/BINX file(s), (ii) list(s) of grains to be included in the modelling (based
125 on pre-defined selection criteria, *e.g.* on recycling and/or recuperation ratios), (iii) file(s) indicating how
126 the data should be processed (signal integration channels, reproducibility of the instrument(s), etc.)



127 and (iv) both natural (in $\text{Gy}\cdot\text{ka}^{-1}$) and laboratory (in $\text{Gy}\cdot\text{s}^{-1}$) dose rates. Based on these data, the
128 calculations are performed all at once using Markov Chain Monte Carlo (MCMC) computations; as a
129 result, unlike in standard frequentist data processing, there is no succession of steps in data analysis
130 (for example, individual equivalent dose estimates are not parameterised, unlike when the CDM is
131 used). While Combès *et al.* (2015) argue that this results in a better statistical inference about the age
132 (or palaeodose), it also comes with a downside: the user cannot visualise the data during the statistical
133 analysis. In particular, the fact that the user must specify the list of grains to be included in the analysis
134 implies that one should always pre-treat the samples in a standard way, by using, *e.g.* *Analyst* (Duller,
135 2015) or the R ‘Luminescence’ package (Kreutzer *et al.*, 2012; Kreutzer *et al.*, 2020) to visually check
136 the data but also investigate the effect of various selection criteria on the datasets (see for example
137 Thomsen *et al.*, 2016, on the effect of applying various selection criteria when with frequentist
138 statistical models; see Heydari and Guérin, 2018, for a similar study in a Bayesian framework).

139 In other words, using ‘BayLum’ for age calculation should not, and does not, prevent the user
140 from a careful and critical examination of the measured OSL data. In particular, before running age
141 calculations using the ‘BayLum’ package, it is important that the user already has identified potential
142 problems – *e.g.*, saturation and/or dose rate variability (see Heydari and Guérin, 2018, for adapted
143 modelling solutions).

144 3. First simple model and output

145 We first ran the function `Generate_DataFile()` for the OSL samples FER 1 and FER 3,
146 with the same lists of grains as those used for age calculation by Guérin *et al.* (2015b): all grains with
147 an uncertainty smaller than 20% on the first test dose signal were selected. A large number of grains
148 appeared to be in saturation for these samples (in *Analyst*, there is no intersection of the natural L/T
149 signal, or the sum of this sensitivity corrected natural signal and its uncertainty, with the dose-response
150 curve). As a result, following Thomsen *et al.* (2016) an additional selection criterion was added, based
151 on the curvature parameter of the dose-response curves. All grains for which the D_0 value, obtained
152 with *Analyst* as described by Guérin *et al.* (2015b), was smaller than 100 Gy, were rejected from the
153 analysis (note however that such a selection criterion may not be necessary when working with
154 ‘BayLum’: Heydari and Guérin, 2018).

155 In practice, the data is contained in two folders named after the samples and provided as
156 Supplementary Material. Each folder contains one BIN/BINX-file (*i.e.* OSL measurements; note that
157 only a small fraction of the measured grains is included here Supplementary Material) and four CSV-
158 files:

- 159 - ‘DiscPos.csv’ lists all selected grains;
- 160 - ‘Rule.csv’ gives the rules for generating L_x/T_x data (integration channels for both the natural
161 or regenerated and test dose signals, uncertainty arising from the reproducibility of the OSL
162 measurements, and number of SAR cycles to remove for curve fitting, if any - it may, for example, be
163 desirable to remove recycled points and/or IR depletion points);
- 164 - ‘DoseSource.csv’ gives the laboratory source dose rate and its variance;
- 165
- 166 - ‘DoseEnv.csv’ gives the dose rate to which the sample was exposed during burial.

167 We ran the function `AgeS_Computation()` with a prior age interval limited to between
168 10 ka and 100 ka for each sample (so that the bounds are far from the age values obtained using
169 arithmetic mean of equivalent doses, namely 37 ± 2 ka and 40 ± 2 ka, respectively). The dose-response



170 curves were fitted, as in *Analyst* in our previous study, with single saturating exponential functions
171 passing through the origin. All uncertainties, affecting both environmental and laboratory dose rates,
172 were included in the calculation, as is common practice in luminescence dating; however, the
173 covariance of ages was not modelled here, so the results are equivalent to those one would obtain by
174 running subsequent individual age calculations for each of the two samples.

175 To run the `AgeS_Computation()` function, the user must choose a model for the
176 distribution of individual equivalent doses around the central dose; the different options are Cauchy,
177 Gaussian or lognormal distribution (in the latter case, the central dose may be estimated either by the
178 mean or the median of the distribution). On top of saturation problems, Guérin *et al.* (2015b) also
179 identified dose rate variability as an important factor of dispersion in equivalent doses: the values of
180 the CDM overdispersion parameter for the D_e distributions of the samples were equal to $29 \pm 3\%$ and
181 $35 \pm 3\%$, respectively. Consequently, to avoid problems of age underestimation, following the results
182 of laboratory-controlled experiments of Heydari and Guérin (2018), we did not use the Cauchy
183 distribution model. Instead, we modelled the equivalent dose distribution by a lognormal distribution
184 (one could also have chosen a Gaussian function) from which the mean (rather than the median) was
185 used to estimate the central dose. Indeed, Guérin *et al.* (2017) formally demonstrated that the median
186 of the lognormal distribution (as used in the CDM) is a biased estimator and leads to age
187 underestimates when dose rates are dispersed (see Heydari and Guérin, 2018, for experimental
188 confirmation of this demonstration).

189 After 5,000 iterations of 3 independent Markov Chains, we observed good convergence, as
190 seen in the Markdown document provided as supplementary material (for a discussion of the
191 convergence of the Markov Chains, the reader is referred to Philippe *et al.*, 2019). The upper limit of the
192 95% Credible Intervals (C.I.) for the Gelman and Rubin indexes of convergence (Gelman and Rubin,
193 1992) were all smaller than 1.05, also indicating satisfying convergence of the 3 independent Markov
194 Chains (here again, the reader is referred to Philippe *et al.*, 2019, who suggested 1.05 as the maximum
195 acceptable value). The obtained 95% C.I. for the ages of samples FER 1 and FER 3 are [34.1; 43.3] ka
196 and [36.6; 47.8] ka, respectively (Fig. 1; Table 1) and are consistent with the ages obtained by Guérin
197 *et al.* (2015b) with a much simpler approach (unweighted arithmetic mean of equivalent doses). It
198 should be emphasised here that the two 95% C.I. for ages overlap. Fig. 2 shows a bivariate scatter plot
199 of a sample of observations from the joint posterior distribution of the two ages, as generated by the
200 Markov Chains; in such a plot, each point corresponds to one realisation of the ages of the two samples
201 investigated in the MCMC. Fig. 3 shows the corresponding probability densities for the ages estimated
202 jointly, based on kernel density estimates (KDE), and the marginal probability densities. No correlation
203 is observed on the joint probability density, which is symmetrical and bell-shaped. One can already
204 compare here the results obtained with this Bayesian model (lognormal-average) for sample FER 3
205 with the radiocarbon ages obtained independently for the same layer by Guérin *et al.* (2015b). The
206 95% C.I. for the 3 ^{14}C ages are bound by the interval [44.4; 47.3] ka, which means that the OSL and
207 radiocarbon ages are in good agreement, which was not the case when calculating the ages with the
208 CDM (38 ± 2 ka). Thus, even without further modelling, the 'BayLum' lognormal-average model seems
209 to provide OSL ages in better agreement with radiocarbon.

210 4. Stratigraphic constraints

211 Samples FER 1 and 3 belong to two different stratigraphic layers: sample FER 1 (Layer 7) lies
212 above sample FER 3 (Layer 5B), so we know that the age of sample FER 1 must be less than that of
213 sample FER 3. To encode this information, the function `AgeS_Computation()` takes as argument
214 the object `StratiConstraints`, which is a matrix whose size depends on the number of analysed
215 samples. First, the data in the `DATA` object (which is the output of the function



216 `Generate_DataFile()` must be ordered in stratigraphic order from top to bottom: thus, in our
217 case the list of names used by the function `Generate_DataFile()` is FER 1, FER 3 (rather than FER
218 3, FER 1). Then, the stratigraphic matrix contains numbers equal to 0 or 1 indicating the applied bounds
219 to the age of each sample. The matrix contains a number of rows equal to the number of samples plus
220 one and a number of columns equal to the number of samples. The first row only contains 1 values,
221 which indicates that the lower age bound specified as prior information (10 ka in our example, cf.
222 section 3 above) when running the function `AgeS_Computation()` applies to all samples. Then,
223 for all j in $\{2, \dots, Nb_Sample+1\}$ and all i in $\{j, \dots, Nb_Sample\}$, `StratiConstraints[j,i]=1` if the
224 age of sample whose number ID is equal to $j-1$ is smaller than the age of sample whose number ID is
225 equal to i . Otherwise, `StratiConstraints[j,i]=0`. In practice, in our case
226 `StratiConstraints [1,] = (1,1)`, `StratiConstraints [2,] = (0,1)` (which means that
227 the age of sample FER 1 is not less than itself but is less than that of sample FER 3) and
228 `StratiConstraints [3,] = (0,0)` (which means that sample FER-3 is neither younger than
229 sample FER-1 nor itself). Note: in the markdown document provided as Supplementary Material, the
230 corresponding code lines are commented and perhaps make this description easier to follow.

231 Running the function `AgeS_Computation()` with this matrix of stratigraphic constraints
232 only marginally affects the ages, in this case, the 95% C.I. become [34.3; 42.9] ka and [38.1; 48.5] for
233 samples FER-1 and FER-3, respectively (Table 1). One can also look at the bivariate scatter plot of
234 observations from the joint posterior distribution (Fig. 4): one can see that this scatter plot is truncated
235 in the upper left-hand corner – illustrating the fact that the age of sample FER 1 can never be greater
236 than that of sample FER 3 (see Fig. 2 for comparison). By contrast, the KDE estimate (Fig. 5) also shows
237 a positive correlation but does not reveal the truncation (whereas the stratigraphic constraint imposes
238 a null probability for all pairs of ages above the 1:1 line).

239

240 5. Dealing with multiple sources of errors through a covariance matrix

241 5.1. General considerations

242 In the previous calculations, all the variance is treated as random, whereas common, systematic errors
243 should not allow solving stratigraphic inversions (they affect all ages in the same direction, although
244 to varying degrees). One of the main advantages of applying the models implemented in the ‘BayLum’
245 package – contrary to other chronological modelling tools such as *OxCal* (Bronk Ramsey and Lee, 2013)
246 or *Chronomodel* (Lanos and Philippe, 2018) – lies in the possibility to include the structure of
247 uncertainties specific to OSL dating. For instance, a radiocarbon age is derived only from the ratio of
248 ^{14}C to ^{12}C (on top of which comes the more complex problem of calibration), whereas an OSL age
249 involves a large number of measurements, each with its uncertainty (Aitken, 1985; 1998). The OSL
250 measurements required for the determination of the palaeodose are relatively standardised through
251 the widespread use of the SAR protocol (Murray and Wintle, 2000; Wintle and Murray, 2006).
252 Conversely, there are several approaches – each with its equipment and standards – to determine the
253 various dose rate components. Given that these dose rates derive from different types of radiation
254 (alpha, beta, gamma and cosmic radiation) and are of various origins (mainly from potassium and the
255 uranium and thorium radioactive chains), there are many more contributions to the age uncertainty
256 from the dose rate term than from the palaeodose term, even though the size of the uncertainty on
257 dose rate is of the same order of magnitude as that on palaeodose – see for example Murray *et al.*,
258 2015). As a result, there are almost as many ways of estimating systematic and random uncertainties
259 as there are (combinations of) ways to determine dose rates. Combès and Philippe (2017) detailed the
260 mathematical formulation of the dose covariance matrix, which links the ages of several samples



261 measured using the same equipment and standards through common (systematic) errors (see also
262 Philippe *et al.*, 2019). Nevertheless, the equations provided in this article are somewhat difficult to
263 translate in practice; here, we propose to outline how we implement a covariance matrix adapted to
264 (one example of) the measurements leading to OSL age calculation at the IRAMAT-CRP2A laboratory
265 (Bordeaux). We emphasise that what follows is not prescriptive; it should be viewed as an example of
266 a model of uncertainties. For alternative ways of estimating systematic and random errors, for
267 example, due to different measurements of dose rates, the reader is referred to the discussion (section
268 7.1).

269 Here, we consider the case of a series of n sediment samples taken from one unique site and all
270 measured using the same equipment and standards. Let us consider the following relationship
271 between palaeodoses, dose rates and ages (Combès and Philippe, 2017):

$$272 \quad (D_1, \dots, D_n) \sim \mathcal{N} \left((A_1 \dot{d}_1, \dots, A_n \dot{d}_n), \Sigma \right)$$

273 where D_i is a random variable modelling the unknown palaeodose of sample i , \mathcal{N} is the symbol for a
274 Gaussian distribution, A_i is the unknown age estimate of sample i (that we are trying to determine),
275 \dot{d}_i the total dose rate to which this sample was exposed since burial (\dot{d}_i is the observed dose rate, *i.e.*
276 the result of the measurements) and Σ is the dose covariance matrix (for the full definition of the
277 model, we refer the reader to Combès and Philippe, 2017). This covariance matrix verifies, for all (i,j) :

$$278 \quad \Sigma_{i,j} = A_i A_j \theta_{i,j} \quad (\text{Eq. 1})$$

279 where θ is the matrix, the user needs to specify to run the calculations with 'BayLum'. It should be
280 noted here that by default when running age calculations with 'BayLum', the off-diagonal elements
281 are set to zero, *i.e.* the covariance in ages is not modelled.

282 Before entering the details specific to luminescence dating, let us consider a simple example of two
283 measurements $y_1 = \mu_1 + e_1 + f$ and $y_2 = \mu_2 + e_2 + f$ where μ_1 and μ_2 are fixed measurands and e_1 , e_2 and
284 f are all independent random errors from distributions with mean zero. The covariance of y_1 and y_2 is
285 the variance of f (so the off-diagonal elements of the matrix are equal to this variance). For each
286 sample, the diagonal element of the corresponding covariance matrix is the sum of all the components
287 of variance for that sample. The variety of physical quantities to measure to determine dose rate, and
288 their relationship with the dose rate contributions, will now be discussed with this simple definition in
289 mind.

290 **5.2. Implementation in practice**

291 First, we detail the series of measurements carried out, and we introduce the corresponding
292 notations for the estimates and associated uncertainties. Table 2 summarises all physical units and
293 associated error standard deviations; as a general rule, we assume that all error terms are Gaussian
294 variables with the expected value (mean) equal to zero and a fixed, known standard deviation (see for
295 example Eq. 2 in Combès and Philippe, 2017). For clarity, in the following relative standard deviations
296 are described by the letter σ , while absolute standard deviations are denoted by s ; moreover, each
297 standard deviation corresponding to random errors (*i.e.*, when the error varies from sample to sample)
298 is identified by the letter i in the subscript. The absence of this letter in the subscript indicates that the
299 measurement error affects all samples.

300 **5.2.1. Equivalent doses and OSL measurements**

301 Equivalent doses are determined from OSL measurements performed on a luminescence
302 reader equipped with a radioactive beta source, whose dose rate and associated relative standard



303 deviation of the error, noted \hat{d}_{lab} and σ_{lab} , are known. There are several ways the latter term can be
304 determined; in its simplest form, it includes the standard deviation of the error on the absolute dose
305 absorbed by the standard reference material (in our case calibration quartz provided by DTU Nutech,
306 *cf.* Hansen *et al.*, 2015) and an error term due to replicate measurements of several aliquots of this
307 calibration material. Using a large number of measurements repeated in time, as suggested by Hansen
308 *et al.* (2015), may somewhat complicate the matter, but this goes beyond the scope of the present
309 study.

310 In practice, regeneration doses are delivered by irradiating the aliquots for a given duration (in
311 s). This duration is converted to absorbed energy dose (Gy) by multiplication with the source dose rate
312 ($Gy \cdot s^{-1}$). Strictly speaking, the error on the source dose rate affects all regeneration doses, and so this
313 error term should appear in the dose/luminescence relationship (right side of the directed acyclic
314 graph shown in Fig. 7 of Combès and Philippe, 2017). However, it is common practice in the field of
315 luminescence dating to first calculate an equivalent dose in seconds of irradiation for each aliquot,
316 then convert this to Gy and calculate an average (or determine another central parameter such as with
317 the CDM), and only then consider σ_{lab} . This is what led, *e.g.*, Jacobs *et al.* (2008), to exclude the
318 associated standard deviation from the total OSL age uncertainties, to test the assumption of a time
319 gap between two series of ages. Here, for simplicity, we take the same route, and hence the relative
320 error on the laboratory source dose rate becomes a relative, systematic error on the equivalent doses.

321 One may thus write that the error on the dose D_i arising from the calibration of the source
322 follows a Gaussian distribution with mean 0 and variance $(\sigma_{lab} A_i \hat{d}_i)^2$.

323

324 5.2.2. Dose rates

325 When it comes to the dose rate term, here we restrict ourselves to the case of coarse quartz
326 grains measured after HF etching to remove the alpha dose rate component: the total natural dose
327 rate is the sum of an internal dose rate, external beta and gamma dose rates, and cosmic dose rates.

328 Cosmic dose rates

329 We consider that cosmic dose rates are determined following Prescott and Hutton (1994)
330 based on the burial depth of the dated samples, which may be different from the present-day thickness
331 of the overburden. As a result, the error on cosmic dose rate estimates depends on the error
332 estimation of this effective burial depth since the dated sediment was deposited. Because the
333 relationship between cosmic dose rates and burial depths is not linear, and because the error on this
334 burial depth may not be systematic (*e.g.* in cases where successive, yet of unknown duration, erosion
335 and deposition events happened between the deposition of superimposed sedimentary layers – see
336 Aitken, 1998, p. 65, for a discussion) even at the scale of a site the error associated to cosmic dose
337 rates cannot easily be treated as systematic. For $i=\{1, \dots, n\}$, $\hat{d}_{cosmic,i}$ and $s_{cosmic,i}$ denote the estimate
338 of the average cosmic dose rate to which sample i has been exposed and its associated standard
339 deviation.

340 Beta dose rates

341 We consider the beta dose rates as determined from concentrations (or activities) of ^{40}K and
342 in radioelements from the U- and Th- decay chains, converted to dose rates using specific conversion
343 factors (*e.g.*, Guérin *et al.*, 2011). At the IRAMAT-CRP2A laboratory, these concentrations are usually
344 determined with low-background, high-resolution gamma-ray spectrometry following Guibert and
345 Schvoerer (1991). The simplest case is that of ^{40}K , since only one peak is used (at 1.461 MeV); the



346 concentration in sample i , denoted $[K]_i$ is equal to the concentration in the standard multiplied by the
347 ratio in count rates (the count rate observed for the investigated sample is divided by the count rate
348 observed for a reference material). Thus, we consider in this paper that the standard deviation of the
349 error on the ^{40}K concentration includes three components: the standard deviation of the error on the
350 concentration in the standard, and the counting uncertainties both on the standard and on the
351 measured sample. The counting uncertainties are calculated, assuming Poisson statistics. Of these
352 three sources of errors, only one is treated as random – namely the counting uncertainty of the sample;
353 the other two standard deviations (corresponding to the counting of the standard and to the error of
354 the radioelement concentration in the standard) are quadratically summed and considered as a
355 systematic source of error. One considers for sample i the beta dose rate from potassium $\dot{d}_{\beta,K,i}$ – after
356 correction for grain size-dependent attenuation using the factors from Guérin *et al.*, (2012a); and for
357 moisture content following Nathan and Mauz (2008) (see the discussion section below regarding
358 uncertainties on these correction factors). Neglecting uncertainties in the dose rate conversion factors,
359 we call $\sigma_{K,i}$ the relative random standard deviation of the error on the ^{40}K concentration; its systematic
360 counterpart σ_K is common to all samples. It should be emphasised here that systematic errors on
361 radioelement concentrations, although being shared by all samples, will affect all ages in the same
362 direction but not necessarily by the same amount (even in relative terms, contrary to the error on
363 laboratory beta source calibration) because the relative contribution of beta dose rate from potassium
364 to the total dose rate may vary from one sample to another. The beta dose rates from the U- and Th-
365 series come from a number of radioelements in the corresponding chains; here, for simplicity we
366 consider each series to be in secular equilibrium (this is generally the case for ^{232}Th but may not be
367 true for the U-series, see, *e.g.* Guibert *et al.*, 1994; 2009; Lahaye *et al.*, 2012). Thus, for each sample,
368 the concentrations in ^{238}U and ^{232}Th are converted to dose rate contributions denoted $\dot{d}_{\beta,U,i}$ and
369 $\dot{d}_{\beta,Th,i}$. In contrast to the case of ^{40}K , the analysis of the high-resolution spectra for these radioactive
370 chains is based on a number of primary gamma rays; more specifically, a weighted mean of the
371 concentrations determined from each ray included in the analysis (after taking interference into
372 account) is calculated to estimate the concentration of U (resp. Th). As a result, the standard deviations
373 of the errors on these concentrations are the contributions of two sources: the relative standard
374 deviation on the concentrations of the standards correspond, on the one hand, to systematic sources
375 of errors and are denoted σ_U and σ_{Th} ; conversely, all other relative standard deviations (arising from
376 the counting of the standards and of the sample) are treated as random and denoted $\sigma_{U,i}$ and $\sigma_{Th,i}$.

377 Internal dose rates

378 Unless the internal radioelement concentration is experimentally determined (in which case
379 one needs to consider both systematic and random sources of error for each sample, as is done for
380 beta dose rates), some have suggested using a fixed internal dose rate of $0.06 \pm 0.03 \text{ Gy}\cdot\text{ka}^{-1}$ (Mejdahl,
381 personal communication to Murray, based on Mejdahl, 1987). In this case, we may assume that the
382 dated quartz grains are all of the same origin, and have the same internal radioelement concentration;
383 as a result, we associate a systematic standard deviation s_{int} with the internal dose rate \dot{d}_{int} .

384 Gamma dose rates

385 Gamma dose rates $\dot{d}_{\gamma,i}$ may be determined, as beta dose rates, from K, U and Th
386 concentrations in the sediment. In this case, the reader is referred to the corresponding section above.
387 However, it is relatively frequent, in the case of heterogeneous configurations at the 10 cm scale, that
388 gamma dose rates received by the samples do not correspond to the infinite matrix gamma dose rates
389 of the samples (see for example large gamma dose rate variations at the interface between sediment
390 and bedrock in a cave reported by Guérin *et al.*, 2012b: Fig. 7). In such contexts, gamma dose rates



391 may be determined by *in situ* measurements with Al₂O₃:C artificial dosimeters: these dosimeters are
392 measured with green-light stimulation and their calibration is based on a block of homogeneous bricks
393 located in the basement of IRAMAT-CRP2A (Richter *et al.*, 2010; Kreutzer *et al.*, 2018). Two sources of
394 relative errors are taken into account: a random standard deviation ($\sigma_{\gamma,i}$) accounting for measurement
395 uncertainties, and a shared calibration error including both standard deviations on (i) the true gamma
396 dose rate in the block of bricks and on (ii) the measurement of the dosimeters irradiated inside the
397 block for calibration of the source (σ_{γ}).

398 **Water content**

399 To account for the effect of water on dose rates, one commonly considers the following
400 equation (Zimmerman, 1971; Aitken, 1985):

$$401 \quad \dot{d}_{\beta,i} = \frac{\dot{d}_{\beta,i,dry}}{1+x_{\beta}WF_i},$$

402 where $\dot{d}_{\beta,i,dry}$ is the beta dose rate in the dry sediment, WF_i represents the effective mass fraction of
403 water in the sediment during burial, and x_{β} is a water correction coefficient accounting for the fact
404 that water absorbs more beta dose than typical sedimentary elements, due to lower atomic numbers
405 (Nathan and Mauz, 2008). A similar equation applies to gamma dose rates, with a corresponding factor
406 x_{γ} (see Guérin and Mercier, 2012). The determination of the water content in the sediment over time
407 is a very difficult task as it involves many different parameters, including past rainfall. One commonly
408 employed solution is to measure the water content at the time of sampling and assume it to be
409 representative of that in the past; measuring the water content at saturation may then be a solution
410 to evaluate an upper limit to this value; and depending on the context one may also propose a lower
411 limit to the water content. One then obtains a way of quantifying the standard deviation of the error
412 on the water content, although necessarily imperfect (see Nelson and Rittenour, 2015, for a
413 discussion). Neglecting uncertainties on the water correction factors (x_{β} and x_{γ}) and calling $s_{WF,i}$ the
414 absolute standard deviation of the mass fraction WF_i for sample i , one may write:

$$415 \quad s_{\beta,H_2O,i} = \dot{d}_{\beta,i} \frac{s_{WF,i}}{1+x_{\beta}WF_i}$$

416 where $s_{\beta,H_2O,i}$ is the standard deviation of the beta dose rate for sample i due to the uncertainty on
417 its water mass fraction.

418 Similarly, one may write:

$$419 \quad s_{\gamma,H_2O,i} = \dot{d}_{\gamma,i} \frac{s_{WF,i}}{1+x_{\gamma}WF_i}$$

420 where $s_{\gamma,H_2O,i}$ is the standard deviation of the gamma dose rate for sample i due to the uncertainty on
421 its water mass fraction. As a result,

$$422 \quad s_{\gamma,H_2O,i} = \frac{\dot{d}_{\gamma,i} 1+x_{\beta}WF_i}{\dot{d}_{\beta,i} 1+x_{\gamma}WF_i} s_{\beta,H_2O,i}.$$

423 To simplify the following equations, which are meant to be those used in practice, we introduce the
424 relative standard deviation of the beta dose rate due to water content errors ($\sigma_{\beta,H_2O,i}$) and a parameter
425 called λ_i defined by:

$$426 \quad \lambda_i = \frac{1+x_{\beta}WF_i}{1+x_{\gamma}WF_i}$$



427 **The θ matrix**

428 With these considerations in mind on errors and their nature, the corresponding θ matrix (Eq.
 429 1) to model these uncertainties is a square matrix containing one line (and column) per sample. The
 430 diagonal elements correspond to the sum of a term arising from the error on the laboratory source
 431 dose rate ($\dot{d}_i^2 \sigma_{\text{lab}}^2$) and the total dose rate variance for each sample, for each i :

$$432 \quad \theta_{i,i} = \dot{d}_i^2 \sigma_{\text{lab}}^2 + s_{\text{cosmic},i}^2 + \dot{d}_{\beta,U,i}^2 (\sigma_{U,i}^2 + \sigma_U^2) + \dot{d}_{\beta,K,i}^2 (\sigma_{K,i}^2 + \sigma_K^2) + \dot{d}_{\beta,\text{Th},i}^2 (\sigma_{\text{Th},i}^2 + \sigma_{\text{Th}}^2) + s_{\text{int}}^2$$

$$433 \quad + \dot{d}_{\gamma,i}^2 (\sigma_{\gamma,i}^2 + \sigma_{\gamma}^2) + (\dot{d}_{\beta,U,i} + \dot{d}_{\beta,K,i} + \dot{d}_{\beta,\text{Th},i} + \lambda_i \dot{d}_{\gamma,i})^2 \sigma_{\beta,\text{H}_2\text{O},i}^2.$$

434 This long list of variance terms may seem rather complicated, but it corresponds to the total variance
 435 arising from the laboratory beta source calibration, the errors on cosmic dose rates, environmental
 436 beta dose rates internal dose rates, gamma dose rates, and finally the error arising from uncertainties
 437 in water content. In other words, we can also write

$$438 \quad \theta_{i,i} = \dot{d}_i^2 \sigma_{\text{lab}}^2 + s_{\dot{d}_i}^2 \quad (\text{Eq. 2}),$$

439 where $s_{\dot{d}_i}^2$ is the variance of the dose rate to which sample i was exposed to during burial (it is the
 440 square of the uncertainty appearing next to the dose rate value in every luminescence dating article;
 441 in our example, this term is the second one in the files DoseEnv.csv provided in Supplementary
 442 Material).

443 Then, for $i \neq j$:

$$444 \quad \theta_{i,j} = \dot{d}_{\gamma,i} \dot{d}_{\gamma,j} \sigma_{\gamma}^2 + \dot{d}_{\beta,U,i} \dot{d}_{\beta,U,j} \sigma_U^2 + \dot{d}_{\beta,K,i} \dot{d}_{\beta,K,j} \sigma_K^2 + \dot{d}_{\beta,\text{Th},i} \dot{d}_{\beta,\text{Th},j} \sigma_{\text{Th}}^2 + s_{\text{int}}^2 + \dot{d}_i \dot{d}_j \sigma_{\text{lab}}^2 \quad (\text{Eq. 3}),$$

445 which characterises the amount of correlation between the doses of samples i and j , multiplied by their
 446 ages. The θ matrix, like the dose covariance matrix Σ , is a symmetric matrix. The diagonal members
 447 correspond to individual variances, while the non-diagonal terms express the fact that systematic,
 448 shared errors link the measurements of the series of samples. As a result, running the functions
 449 `AgeS_Computation()` and `Age_OSLC14()` with a θ matrix in which all non-diagonal members
 450 are set to zero would be equivalent to running the same functions without the correlation matrix, or
 451 running the function `Age_Computation()` independently for each sample – in which case all
 452 sources of error are treated as random.

453 **5.3. Examples**

454 **5.3.1. An illustrative, simplistic example without stratigraphic constraints**

455 For illustration purposes, first, we did not apply stratigraphic constraints. We started with a
 456 simplistic θ matrix containing in the diagonal the real error variances (Eq. 2) as determined by Guérin
 457 *et al.* (2015); the σ_{lab} value was equal to 0.02 (2% relative standard deviation of the calibration of the
 458 laboratory beta source). The simplification comes from the off-diagonal members, for which in Eq. (3)
 459 we set all s and σ values equal to 0, except for the σ_{lab} value, set to 0.05. Obviously, this is not self-
 460 consistent, but it corresponds to (i) random and systematic errors of approximately the same
 461 magnitude (in practice, these two sources of errors are of the same order of magnitude – a few %) and
 462 (ii) the simplest form of systematic errors. Indeed, in such a case, all ages are affected by the same
 463 relative amount in the same direction.

464 Here again, after 5,000 iterations of 3 independent Markov Chains, we observed good
 465 convergence. The obtained 95% C.I. are [33.9; 43.8] and [36.7; 48.1] ka for samples FER 1 and FER 3,
 466 respectively. Fig. 6 shows bivariate scatter plots corresponding to the sampling of the Markov Chains



467 for the ages of samples FER 1 and FER 3 (which are calculated simultaneously) and Fig. 7 displays the
468 KDE together with the marginal probability densities. This set of figures illustrate the reason for the
469 generation of the two type of figures: the bivariate scatter plot is most appropriate to visualise the
470 effect of stratigraphic constraints (Fig. 4 above), whereas probability density figures best illustrate the
471 effect of modelling systematic errors. Indeed, as can be seen, there is a positive correlation between
472 the ages of samples FER 1 and FER 3: the greater the age of sample FER 1, the greater is the mean age
473 of sample FER 3. In other words, if the age of sample FER 1 was underestimated, then in all likelihood,
474 so would be the age of sample FER 3. Furthermore, the length of the C.I. for the age of each sample is
475 slightly larger than without modelling the covariance (*cf.* Table 1), *i.e.* modelling the covariances
476 slightly increases the age uncertainties. However, the positive correlation of ages has other, direct
477 consequences.

478 First, let us suppose that we have no knowledge of a stratigraphic link between the two
479 investigated samples, and wish to test the hypothesis that sample FER 1 is younger than sample FER 3.
480 The credibility of such an assumption can be tested using the function `MarginalProbability()`
481 of the 'Archaeophases' R package (Philippe and Vibet, 2020) devoted to the analysis of MCMC chains
482 for chronological inference. Without using the covariance matrix, the credibility of this hypothesis is
483 0.83; with the simplistic θ matrix, the credibility becomes 0.94; in other words, modelling the age
484 covariance reflects more faithfully the measurements and their uncertainties for such tests.

485 The second consequence concerns the duration of a hypothetical phase that would encompass
486 the deposition of sample FER 1 and that of sample FER 3. Indeed, since the ages vary together in the
487 MCMC, the duration of such a phase should be smaller when modelling the covariance than when all
488 the variance in ages is treated as random. Indeed, we could verify this assertion using the function
489 `PhaseStatistics()` of 'ArchaeoPhases' (Philippe and Vibet, 2020): with the simplistic covariance
490 matrix, the 95 % C.I. for the duration of this phase is [-1.4; 9.7] ka, whereas it is [-0.6; 7.6] ka when the
491 ages are calculated using the simplistic θ matrix.

492 5.3.2. A real example, including stratigraphic constraints

493 In a real case, since the relative contributions of the different dose rate components vary from
494 one sample to another, the correlation will be less pronounced. For more realistic calculations of the
495 ages of samples FER 1 and FER 3, we took the same values as above for the diagonal terms of the θ
496 matrix (Eq. 2); on the other hand, for the non-diagonal, covariance terms, we used the following values:
497 $\sigma_{lab} = 0.02$ (which corresponds to the experimentally determined calibration standard deviation,
498 including the uncertainty of the dose delivered to calibration quartz; Hansen *et al.*, 2015), $\sigma_K = 0.012$,
499 $\sigma_U = 0.007$, $\sigma_{Th} = 0.007$ (for these values, which also include counting of the standards used, the
500 reader is referred to Guibert *et al.*, 2009; Guibert, 2002), and $s_{int} = 0.003 \text{ Gy.ka}^{-1}$. We provide as
501 Supplementary Information a calculation spreadsheet allowing to build the covariance matrix,
502 intended for adaptation to the user-specific needs.

503 At the site of La Ferrassie, the uncertainties associated with the gamma dose rate observations
504 are more complex. $\text{Al}_2\text{O}_3\text{:C}$ dosimeters were placed at the end of 25 cm long aluminium tubes and
505 inserted horizontally in the stratigraphic section at the location of sediment sampling. In an ideal case,
506 sediment should be uniform in a horizontal plane; however, for samples FER 1 and FER 3 only a rather
507 thin layer of sediment remained against the cliff wall (the layers of the sample were not present at the
508 site in any other location), which resulted in the dosimeters being inserted either in the karstic cliff
509 (the limestone contains little radioelements compared to the sediments, as shown in Fig. 5 of Guérin
510 *et al.*, 2015b) or at the interface between the cliff and the sediment. As a result, we took for $\dot{d}_{\gamma,i}$ the
511 average between the gamma dose rates measured *in situ* (which underestimate the real gamma dose



512 rate because the effect of the cliff is over-represented) and the gamma dose rates derived from the K,
513 U and Th concentrations in the samples. The associated standard deviation, $\sigma_{\gamma,i}$, was calculated as the
514 difference between these two extreme values divided by 4, so that the 95% C.I. covers all possible
515 values. As this standard deviation is much larger than the analytical uncertainties, we neglected the
516 latter and considered $\sigma_{\gamma,i}$ to characterise random sources of errors since each sample has a different
517 environment and may be more or less far from the cliff.

518 The samples FER 1 and FER 3 are directly above and below, respectively, the Châtelperronian
519 layer at the site (layer 6). Sample FER 2 from this layer being poorly bleached, it is at present impossible
520 to model with 'BayLum'. However, an alternative to estimate the age of FER 2 consists of supposing
521 that it has a uniform prior probability density between the ages of samples FER 1 and FER 3:

$$522 \quad P(A_2|data) \sim \iint \frac{\mathbb{I}_{[A_1;A_3]}}{A_3 - A_1} \pi(A_1, A_3|data) dA_1 dA_3$$

523 where A_i is the age of sample i , $\mathbb{I}_{[A_1;A_3]}$ is the indicator function between A_1 and A_3 , and
524 $\pi(A_1, A_3|data)$ is the posterior joint density of A_1 and A_3 knowing the data (*i.e.* the density estimated
525 with 'BayLum'). Doing so (see the markdown file for the corresponding code lines), working from the
526 output of 'BayLum' one obtains a 95% C.I. of [36; 46] ka, which can be compared with the confidence
527 interval of [36; 48] ka obtained by Guérin et al. (2015) with minimum age modelling.

528 6. Integration of independent chronological data (radiocarbon)

529 The 'BayLum' package also offers the possibility to include radiocarbon ages in the chronological
530 models (Philippe *et al.*, 2018); more specifically, radiocarbon ages are calibrated within 'BayLum', using
531 the function `AgeC14_Computation()` or `Age_OSLC14()` (in the latter case the function
532 necessitates at least one OSL age calculation). Introducing covariance matrices to account for
533 systematic errors on OSL data does not reduce the OSL age uncertainties; however, it becomes
534 particularly useful to correct for estimation biases when more precise ages, unaffected by these
535 systematic errors, are integrated into the models. To illustrate this, we decided to construct two
536 models constraining the age of FER 3; for illustration purposes, in this section, we used the simplistic
537 θ matrix described above in section 5.3.1. In the first case, we constrained the age of this sample by
538 imposing that a 'young' radiocarbon age (young compared to the age of sample FER 3 considered
539 alone) has an age greater than sample FER 3. In practice, we arbitrarily took a radiocarbon age of
540 $38,000 \pm 400$ BP, which corresponds to [37.6; 39.9] ka cal. BP (95% C.I. using the IntCal20 curve, Reimer
541 *et al.*, 2020; the calibration was performed using 'BayLum', see Philippe *et al.*, 2018). Naturally, the
542 credible intervals (both 68% and 95%) for sample FER 3 are shifted towards younger age values (*cf.*
543 truncation of the scatter plot illustrated in Fig. 3). So do the credible intervals for sample FER 1, since
544 the ages of the two OSL samples are close to each other even when considered independently of
545 radiocarbon data (in other words, the radiocarbon age 'pushes' the age of sample FER 3, which in turn
546 'pushes' the age of sample FER 1). In practice, the 95% C.I. become [33.3; 41.2] ka and [36.9; 42.3] ka
547 for samples FER 1 and FER 3, respectively. It can be noted here that in such a case the precision of the
548 age of sample FER 3 is increased (*i.e.* the length of the C.I. is much smaller than without the constraining
549 radiocarbon age). More interestingly, in the second case, we constrained the age of sample FER 3 by
550 imposing that an 'old' radiocarbon age (old compared to the age of sample FER 3 considered alone)
551 has an age younger than sample FER 3. In practice we – again, arbitrarily – took a radiocarbon age
552 equal to $44,000 \pm 400$ BP, which corresponds to [45.4; 47.4] ka cal. BP (95% C.I.). Here again, the effect
553 on the age of sample FER 3 is straightforward: the credible intervals are shifted towards older ages
554 (the 95% C.I. for the age of sample FER 3 becomes [45.7; 51.2] ka). Perhaps less intuitive is the effect
555 on the age of sample FER 1, which is not directly constrained by radiocarbon: because the ages of the



556 three samples are estimated jointly, and because of the systematic errors on the OSL ages, the age of
557 sample FER 1 is also shifted towards older ages: the corresponding 95% C.I. becomes [36.7; 45.8] ka.

558 7. Discussion

559 7.1. Differing ways of estimating dose rates

560 Every laboratory uses its specific equipment and calibration standards; if similar equipment as
561 described above is used, then only the values of the different terms need be changed. This case is
562 particularly relevant for equivalent dose measurements, and hence the term σ_{lab} associated with \hat{d}_{lab} .
563 Conversely, for dose rate determination, several other experimental devices and techniques are
564 commonly used. If beta and/or gamma dose rates are determined based on the determination of
565 concentration in K, U and Th, (for example by mass spectrometry, neutron activation, etc.), then the
566 situation is similar as that described for beta dose rates above.

567 Counting techniques (alpha, beta, and gamma in the case of the threshold technique: Løvborg
568 *et al.*, 1974) may also be used for beta and gamma dose rate estimation. In the case of beta counting,
569 the conversion factor from count rate to dose rate depends on the emitting radioelement
570 (Ankjærgaard and Murray, 2007; see also Cunningham *et al.*, 2018). This dependency is a source of
571 error that may not be characterised by a systematic error (so there is no contribution to the dose
572 covariance matrix). The data acquired with field gamma spectrometers may be analysed in two ways:
573 the ‘window’ technique (see, *e.g.*, Aitken, 1985) corresponds to classical spectrometry analysis; in this
574 case, the structure of uncertainties is the same as that for beta dose rates determined from high-
575 resolution gamma spectrometry (Eq. 3). On the other hand, threshold techniques consist of taking
576 advantage of proportionality between gamma dose rates and (i) the number of counts recorded per
577 unit time above a threshold (Løvborg and Kirkegaard, 1974) or (ii) the energy deposited per unit time
578 above a threshold (energy threshold: Guérin and Mercier, 2011; Miallier *et al.*, 2009). In the former
579 case, the conversion from count rate to dose rate depends on the emitting radioelement, so no
580 systematic error term may be isolated. Conversely, in the latter case (energy threshold), this
581 dependency is negligible (Guérin and Mercier, 2011). As a result, the error on the dose rate of the
582 calibration standard may be considered as systematic, and thus contribute one term in the non-
583 diagonal elements of the covariance matrix.

584 7.2. Error terms neglected in this study

585 As mentioned earlier in the section devoted to dose rate uncertainties, there are many
586 possibilities to quantify, but also to consider errors on dose rate measurements; one could mention
587 here the uncertainties on attenuation factors and water correction factors. However, both of these
588 factors are dependent on the infinite matrix assumption: attenuation in grains implies that something
589 other than the grains does not attenuate radiation; water correction factors are often calculated
590 assuming a homogeneous mixture of water and other sedimentary components (Zimmerman, 1971;
591 Aitken and Xie, 1990; note: the composition of the sediment also necessarily affects the ratios of
592 electron stopping powers and photon interaction cross-sections – see Nathan and Mauz, 2008, for a
593 discussion). Limitations of this infinite matrix assumption, which is not met in sand samples at the scale
594 of beta dose rates, have already been pointed out (Guérin and Mercier, 2012; Guérin *et al.*, 2012a;
595 Martin *et al.*, 2015). Consequently, it seems that routine determination of a realistic standard deviation
596 of the attenuation and water content correction parameters is not straightforward.

597 Dose rate conversion factors were assumed above to be known without error; however,
598 estimation errors do affect half-lives, emission probabilities, average emitted energies, etc. Liritzis *et al.*
599 (2013) took these uncertainties into account to estimate standard deviations of the dose rate



600 conversion factors (in practice, these standard deviations amount to ~1% for K dose rates, ~2% for U
601 and ~2% for Th). These standard deviations could be included as sources of systematic errors when the
602 contributions of K, U and Th are determined separately (note: when this is not the case, as when
603 dosimeters are used for gamma dose rate estimation, or when beta counting is implemented for beta
604 dose rate assessment, these sources of errors should be treated as random).

605 In this study, we worked with coarse grain quartz extracts that had been etched with HF to
606 remove the alpha-irradiated part of the grains. This being said, if alpha dose rates are taken into
607 account, then the situation becomes similar to that of beta dose rates treated above; however, the
608 sensitivity to alpha irradiation must then be taken into account. It is rather frequent in such a case to
609 use published values from the literature (e.g., Tribolo *et al.*, 2001; Mauz *et al.*, 2006). Depending on
610 the geological origin of the quartz (one or more sources), one may then assume either systematic or
611 random errors on the alpha sensitivity.

612 **7.3. Publication habits and re-analysis of previously published ages**

613 Compared to other statistical models for OSL dating, the Bayesian models implemented in
614 'BayLum' appear rather complicated, at least partly because modelling starts from the measured OSL
615 data. By comparison, the input data to the CDM or the Average Dose Model (ADM: Guérin *et al.*, 2017)
616 are lists of equivalent doses and associated uncertainties, which means that OSL measurements have
617 already been analysed to derive equivalent doses. Combès *et al.* (2015) argued that their complete
618 model (implemented in 'BayLum'), relating all the variables to one another, produces a more
619 homogeneous and consistent inference compared to consecutive inferences (and indeed, when
620 approaching saturation, *i.e.* when equivalent doses and associated uncertainties can hardly be
621 parameterised, Heydari and Guérin (2018) demonstrated the advantage of 'BayLum' models compared
622 to parametric models such as the CDM and ADM in particular settings. However, working with lists of
623 equivalent doses and uncertainties – or even with estimates of central doses and associated
624 uncertainties – taken as observations would make the Bayesian modelling proposed in 'BayLum' and
625 described in this paper more straightforward and transparent. Such an approach, called the 'two-steps'
626 model by Combès and Philippe (2017; see also Millard 2006a, 2006b, for earlier, similar models), would
627 also offer the advantage of allowing re-analysis of already published data to derive more precise
628 chronologies. However, for this purpose the breakdown of all uncertainties and related standard
629 deviations of errors is needed; nowadays, providing such key information for the modelling is not in
630 the publication habits of the luminescence dating community. That being said, with the growing
631 number of meta-analyses of previously published data, and the availability to use models such as
632 BayLum to combine measurements with systematic errors, these habits might evolve in the future.

633 **7.4. Notes of caution**

634 As always when working with statistical models, one should first and foremost evaluate the
635 measured data in the light of sampling context. We already mentioned the importance of grain
636 selection (section 2.2.); but, perhaps more importantly, and especially since users of 'BayLum' have to
637 make modelling choices (e.g., regarding the dose-response curves fitted to OSL measurements or the
638 distribution of individual equivalent doses around the central dose), it is crucial to carefully examine
639 data and assess their quality before building potentially sophisticated models.

640 We would like here to emphasise a few warnings regarding modelling samples in stratigraphic
641 constraints, and the association of ages obtained by different methods. We would advise users, before
642 combining, e.g. radiocarbon and OSL ages, first to thoroughly examine the corresponding datasets
643 independently: how were the data produced (with which experimental procedure)? Are the provided
644 uncertainties reliable (or is there an unrecognised source of error that should be included in the



645 evaluation of uncertainty)? Users are also encouraged to examine the consistency of results produced
646 by each method, in light of the stratigraphy. In a second stage, before modelling of independent ages,
647 we would recommend assessing the consistency of these datasets – do they (at least broadly) agree?
648 And if not, can a parsimonious explanation be found? For example, it is rather common, when
649 performing Bayesian modelling with tools such as *OxCal*, to observe a large fraction of ages considered
650 as outliers; such observations should urge users to examine their data again and come up with likely
651 explanations (note: to this date, no outlier model has been developed for the OSL ages in ‘BayLum’).

652 When it comes to imposing ordering constraints between ages as a result of stratigraphic observations,
653 it is, of course, essential to leave no doubt about the validity of these stratigraphic constraints (the
654 results of a model depend on the assumptions that are made, and the order in ages is a very strong
655 constraint). Perhaps more importantly, even when stratigraphic constraints are valid, it is possible that
656 applying them will not improve the statistical inference.

657 A simple example to illustrate this point is that of two superimposed, distinct layers (so that a
658 stratigraphic order is clear) whose true ages are equal (or in practice, for which the age difference is
659 negligible compared to the typical uncertainties of the implemented dating method). In such a case,
660 modelling the ages with stratigraphic constraints is likely to result in a loss of accuracy (the age of the
661 older layer will be overestimated, and that of the younger layer underestimated) compared to a model
662 where no stratigraphic constraints are imposed. Future developments of the ‘BayLum’ package might
663 include the possibility to test different modelling scenarios by comparing the agreement between the
664 observations and the posterior probability densities, for example using the Bayes Information Criterion
665 (BIC).

666 **8. Conclusion**

667 New models for building chronologies based on OSL, with the possibility to incorporate radiocarbon,
668 have been proposed in the literature (Combès *et al.*, 2015; Combès and Philippe, 2017). These models
669 have been demonstrated to improve the chronological inference based on OSL data and in particular,
670 the accuracy of OSL ages (Guérin *et al.*, 2015; Heydari and Guérin, 2018). The R package ‘BayLum’ was
671 developed to implement these models; Lahaye *et al.* (2018), Carter *et al.* (2019), Heydari *et al.* (2020)
672 and Heydari *et al.* (in review) have used some of them to establish the chronologies of sedimentary
673 sequences dated by OSL, resulting in generally more precise chronologies.

674 In this article, we have presented a case study on how to build simple models and observe output data,
675 in particular through bivariate plots of age probability densities. Then, we have shown how to include
676 stratigraphic constraints in the models; we have described how to fill the covariance matrices to
677 account for systematic errors in OSL age estimation; and we have shown the effect of including
678 independent age information in the models, namely radiocarbon ages. Different tools to visualise and
679 further analyse the output of ‘BayLum’ were demonstrated.

680 As a result, it is now possible to make use of various information often available in practice when dating
681 stratigraphic sequences. Age inferences based on OSL and independent data (*e.g.*, radiocarbon) in
682 stratigraphic constraints are expected to gain in accuracy, precision and robustness, through the
683 application of such Bayesian models.

684

685 **Acknowledgements**

686 The authors thank Andrew Millard, Rex Galbraith and an anonymous referee for helpful comments on
687 a previous version of this article. This study received financial supports of the Région Aquitaine (in



688 particular through the CHROQUI programme) and of the LaScArBx project (project n° ANR-10-
689 LABX-52). M. Autzen, and J.P. Buylaert received funding from the European Research Council (ERC)
690 under the European Union's Horizon 2020 research and innovation programme ERC-2014-StG 639904-
691 RELOS.

692 **References**

- 693 Aitken, M. J., 1985. Thermoluminescence dating. Academic Press, London, 359 p.
- 694 Aitken M.J., 1998. An introduction to optical dating. Oxford University press, Oxford, 267 p.
- 695 Aitken, M.J. and Xie, J., 1990. Moisture correction for annual gamma dose, *Ancient TL* 8 (2), pp. 6–9.
- 696 Ankjærgaard, C., Murray, A.S., 2007. Total beta and gamma dose rates in trapped charge dating based
697 on beta counting. *Radiation Measurements*, 42, 352-359.
- 698 Bronk Ramsey, C., Lee, S., 2013. Recent and Planned Developments of the Program OxCal.
699 *Radiocarbon*, 55(2-3), 720-730.
- 700 Buck CE, Kenworthy JB, Litton CD, Smith AFM. 1991. Combining archaeological and radiocarbon
701 information: a Bayesian approach to calibration. *Antiquity* 65(249):808–21.
- 702 Bøtter-Jensen, L., Bulur, E., Duller, G.A.T., Murray, A.S., 2000. Advances in luminescence instrument
703 systems. *Radiation Measurements* 32, 523–528.
- 704 Carter, T., Contreras, D. A., Holcomb, J., Mihailović, D. D., Karkanas, P., Guérin, G., Taffin, N.,
705 Athanasoulis, D., Lahaye, C., 2019. Earliest occupation of the Central Aegean (Naxos), Greece:
706 Implications for hominin and *Homo sapiens*' behavior and dispersals. *Science advances*, 5(10),
707 eaax0997.
- 708 Chevrier, .B., Lespez, L., Lebrun B., Garnier, A., Tribolo, C., Rasse, M., Guérin, G., Mercier, N., Camara,
709 A., Ndiaye, M., Huysecom, E. New data on settlement and environment at the 2 Pleistocene/Holocene
710 boundary in Sudano-Sahelian West Africa: 3 interdisciplinary investigation at Fatandi V, Eastern
711 Senegal. *PlosOne*, accepted for publication.
- 712 Christophe, C., Philippe, A., Kreutzer, S., Guérin, S., 2020: 'BayLum': Chronological Bayesian Models
713 Integrating Optically Stimulated Luminescence and Radiocarbon Age Dating. R package, version 0.2.0.
714 <https://CRAN.R-project.org/package=BayLum>
- 715 Christophe, C., Philippe, A., Guérin, G., Mercier, N., Guibert, P., 2018. Bayesian approach to OSL dating
716 of poorly bleached sediment samples: Mixture Distribution Models for Dose (MD²). *Radiation*
717 *Measurements* 108, 59-73.
- 718 Combès, B. and Philippe, A., 2017. Bayesian analysis of individual and systematic multiplicative errors
719 for estimating ages with stratigraphic constraints in optically stimulated luminescence dating,
720 *Quaternary Geochronology*, 39, 24–34.
- 721 Combès, B., Lanos, P., Philippe, A., Mercier, N., Tribolo, C., Guérin, G., Guibert, P., Lahaye, C., 2015. A
722 Bayesian central equivalent dose model for optically stimulated luminescence dating. *Quaternary*
723 *Geochronology* 28, 62-70.
- 724 Cunningham, A.C., Murray, A.S., Armitage, S.J., Autzen, M., 2018. High-precision natural dose rate
725 estimates through beta counting. *Radiation Measurements*, in press.
- 726 Duller, G.A.T., 2015. The Analyst software package for luminescence data: overview and recent
727 improvements. *Ancient TL* 33, 35-42.



- 728 Duller, G.A.T., Bøtter-Jensen, L., Murray, A.S., Truscott, A.J., 1999. Single grain laser luminescence
729 (SGLL) measurements using a novel automated reader. *Nuclear Instruments and Methods B* 155, 506–
730 514.
- 731 Galbraith, R.F., Roberts, R.G., 2012. Statistical aspects of equivalent dose and error calculation and
732 display in OSL dating: An overview and some recommendations. *Quaternary Geochronology* 11, 1-27.
- 733 Galbraith, R.F., Roberts, R.G., Laslett, G.M., Yoshida, H., Olley, J.M., 1999. Optical dating of single and
734 multiple grains of quartz from Jinmium rock shelter, northern Australia: Part I, experimental design
735 and statistical models. *Archaeometry* 41, 339-364.
- 736 Gelman, A., Rubin, D., 1992. Inference from Iterative Simulation using Multiple Sequences. *Statistical*
737 *Science* 7, 457–511.
- 738 Guérin, G., Mercier, N., 2011. Determining gamma dose rates by field gamma spectroscopy in
739 sedimentary media: results of Monte Carlo simulations. *Radiation Measurements*, 46 (2), 190-195.
- 740 Guérin, G., Mercier, N., 2012. Preliminary insight into dose deposition processes in sedimentary media
741 on a grain scale: Monte Carlo modelling of the effect of water on gamma dose-rates. *Radiation*
742 *Measurements*, 47, 541-547.
- 743 Guérin, G., Mercier, N. and Adamiec, G., 2011. Dose-rate conversion factors: update. *Ancient TL* 29, 5-
744 8.
- 745 Guérin, G., Mercier, N., Nathan R., Adamiec, G., Lefrais, Y., 2012a. On the use of the infinite matrix
746 assumption and associated concepts: a critical review. *Radiation Measurements*, 47, 778-785.
- 747 Guérin, G., Discamps, E., Lahaye, C., Mercier, N., Guibert, P., Turq, A., Dibble, H., McPherron, S.,
748 Sandgathe, D., Goldberg, P., Jain, M., Thomsen, K., Patou-Mathis, M., Castel, J.-C., Soulier, M.-C.,
749 2012b. Multi-method (TL and OSL), multi-material (quartz and flint) dating of the Mousterian site of
750 the Roc de Marsal (Dordogne, France): correlating Neanderthals occupations with the climatic
751 variability of MIS 5-3. *Journal of Archaeological Science*, 39, 3071-3084.
- 752 Guérin, G., Combès, B., Lahaye, C., Thomsen, K. J., Tribolo, C., Urbanova, P., Guibert, P., Mercier, N.,
753 Valladas, H., 2015a. Testing the accuracy of a single grain OSL Bayesian central dose model with known-
754 age samples. *Radiation Measurements* 81, 62-70.
- 755 Guérin, G., Frouin, M., Talamo, S., Aldeias, V., Bruxelles, L., Chiotti, L., Dibble, H. L., Goldberg, P., Hublin,
756 J.-J., Jain, M., Lahaye, C., Madelaine, S., Maureille, B, McPherron, S. P., Mercier, N., Murray, A. S.,
757 Sandgathe, D., Steele, T. E., Thomsen, K. J., Turq, A., 2015b. A Multi-method Luminescence Dating of
758 the Palaeolithic Sequence of La Ferrassie Based on New Excavations Adjacent to the La Ferrassie 1 and
759 2 Skeletons, au *Journal of Archaeological Science* 58, 147-166.
- 760 Guérin, G., Jain M., Thomsen K. J., Murray A. S., Mercier, N., 2015c. Modelling dose rate to single grains
761 of quartz in well-sorted sand samples: the dispersion arising from the presence of potassium feldspars
762 and implications for single grain OSL dating. *Quaternary Geochronology* 27, 52-65.
- 763 Guérin, G., Christophe, C., Philippe, A., Murray, A.S., Thomsen, K.J., Tribolo, C., Urbanova, P., Jain, M.,
764 Guibert, P., Mercier, N., Kreutzer, S., Lahaye, C., 2017. Absorbed dose, equivalent dose, measured dose
765 rates, and implications for OSL age estimates: Introducing the Average Dose Model. *Quaternary*
766 *Geochronology* 41, 163-173.
- 767 Guibert, P., 2002. Progrès récents et perspectives. Habilitation à diriger des recherches, 10 juillet 2002.
768 Datation par thermoluminescence des archéomatériaux : recherches méthodologiques et appliquées
769 en archéologie médiévale et en archéologie préhistorique, 3. Université de Bordeaux, pp. 27-50.



- 770 Guibert P. et Schvoerer M., 1991 - TL dating : Low background gamma spectrometry as a tool for the
771 determination of the annual dose, *Nuclear Tracks and Radiation Measurements* 18, 231-238.
- 772 Guibert P., Schvoerer M., Etcheverry M.P., Szepertyski B. et Ney C., 1994. IXth millenium B.C. ceramics
773 from Niger : detection of a U-series disequilibrium and TL dating, *Quaternary Science Reviews*, 13, 555-
774 561.
- 775 Guibert P., Lahaye C., Bechtel F., 2009. The importance of U-series disequilibrium of sediments in
776 luminescence dating: A case study at the Roc de Marsal Cave (Dordogne, France), *Radiation
777 Measurements* 44, 223-231.
- 778 Hansen, V., Murray, A., Buylaert, J. P., Yeo, E. Y., & Thomsen, K., 2015. A new irradiated quartz for beta
779 source calibration. *Radiation Measurements*, 81, 123-127.
- 780 Heydari, M., Guérin, G., 2018. OSL signal saturation and dose rate variability: investigating the
781 behaviour of different statistical models. *Radiation measurements* 120, 96-103.
- 782 Heydari, M., Guérin, G., Kreutzer, S., Jamet, G., Kharazian, M.A., Hashemi, M., Nasab, H.V., Berillon, G.,
783 2020. Do Bayesian methods lead to more precise chronologies? “BayLum” and a first OSL-based
784 chronology for the Palaeolithic open-air site of Mirak (Iran). *Quaternary Geochronology* 59, 101082.
- 785 Heydari, M., Guérin, G., Zeidi, M., Conard, N.J.. Bayesian OSL dating at Ghâr-e Boof, Iran provides a
786 new chronology for Middle and Upper Palaeolithic in the southern Zagros. Submitted to *Journal of
787 Human Evolution*.
- 788 Huntley, D.J., Godfrey-Smith, D.I., Thewalt, M.L.W., 1985. Optical dating of sediments. *Nature* 313,
789 105–107.
- 790 Jacobs, Z., Roberts, R.G., Galbraith, R.F., Deacon, H.J., Grün, R., Mackay, A., Mitchell, P., Vogelsang, R.,
791 Wadley, L., 2008a. Ages for the Middle Stone Age of southern Africa: implications for human behavior
792 and dispersal. *Science* 322, 733-735.
- 793 Kreutzer, S., Schmidt, C., Fuchs, M.C., Dietze, M., Fischer, M., Fuchs, M., 2012. Introducing an R package
794 for luminescence dating analysis. *Ancient TL* 30, 1–8.
- 795 Kreutzer, S., Dietze, M., Burow, C., Fuchs, M. C., Schmidt, C., Fischer, M., Friedrich, J., Mercier, N.,
796 Smedley, R. K., Christophe, C., Zink, A., Durcan, J., King, G.E., Philippe, A., Guérin, G., Riedesel, S.,
797 Autzen, M., Guibert, P., 2020. Luminescence: Comprehensive Luminescence Dating Data Analysis. R
798 package, version 0.9.7. <https://CRAN.R-project.org/package=Luminescence>.
- 799 Kreutzer, S., Martin, L., Guérin, G., Tribolo, C., Selva, P., Mercier, N., 2018. Environmental Dose Rate
800 Determination Using a Passive Dosimeter: Techniques and Workflow for alpha-Al₂O₃:C Chips.
801 *Geochronometria* 45, 56–67.
- 802 Lahaye, C., Guibert, P., Bechtel, F., 2012, Uranium series disequilibrium detection and annual dose
803 determination: A case study on Magdalenian ferruginous heated sandstones (La Honteyre, France),
804 *Radiation Measurements*, 47, 786-789.
- 805 Lahaye, C., Guérin, G., Gluchy, M., Hatté, C., Fontugne, M., Clemente-Conte, I., Santos, J.C., Villagran,
806 X., Da Costa, A., Borges, C., Guidon, N. and Boëda, E., 2018. Another site, same old song: the
807 Pleistocene-Holocene archaeological sequence of Toca da Janela da Barra do Antonião-North, Piauí,
808 Brazil. *Quaternary Geochronology*, in press.
- 809 Lanos, P., Philippe, A., 2018, Event date model: a robust Bayesian tool for chronology building,
810 *Communications for Statistical Applications and Methods*, 25, 1–28.



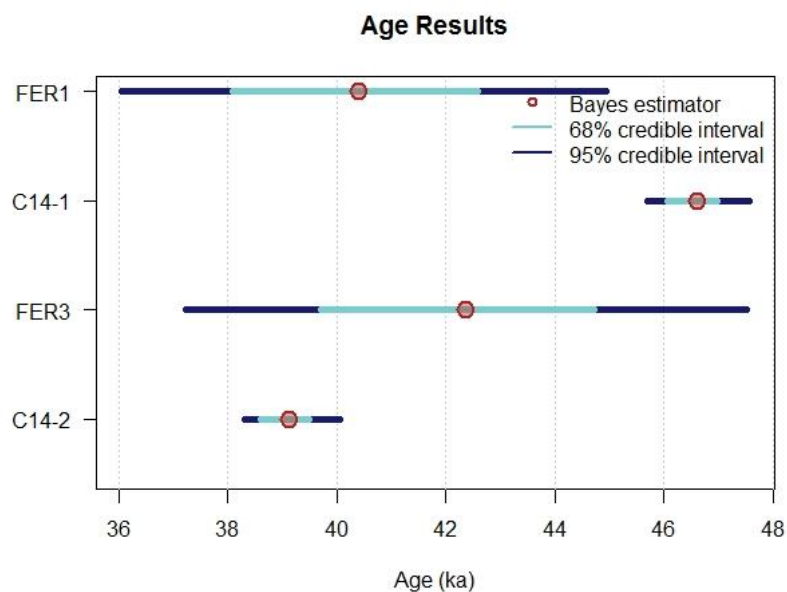
- 811 Liritzis, I., Stamoulis, K., Papachristodoulou, C., Ioannides, K., 2013. A re-evaluation of radiation dose-
812 rate conversion factors. *Mediterranean Archaeology and Archaeometry*, 13, 1-15.
- 813 Løvborg, L., Kirkegaard, P., 1974. Response of 3" x 3" NaI(Tl) detectors to terrestrial gamma radiation.
814 *Nuclear Instruments and Methods* 121, 239-251. Mauz, B., Packman, S. & Lang, A. 2006: The alpha
815 effectiveness in silt-sized quartz: New data obtained by single and multiple aliquot protocols. *Ancient*
816 *TL* 24, 47–52.
- 817 Mejdahl V. 1987. Internal radioactivity in quartz and feldspar grains. *Ancient TL*, 5, 10-17.
- 818 Mercier, N. and Falguères, C., 2007. Field gamma dose rate measurement with a NaI (TI) detector: re-
819 evaluation of the "threshold" technique. *Ancient TL*, 25, 1-4.
- 820 Mercier, N., Kreutzer, S., Christophe, C., Guérin, G., Guibert, P., Lahaye, C., Lanos, P., Philippe, A.,
821 Tribolo, C., 2016. Bayesian statistics in luminescence dating: The 'baSAR'-model and its
822 implementation in the R package 'Luminescence'. *Ancient TL* 34, 14–21.
- 823 Miallier, D., Guérin, G., Mercier, N., Pilleyre, T., Sanzelle, S., 2009. The Clermont radiometric reference
824 rocks: a convenient tool for dosimetric purposes. *Ancient TL*, 27 (2), 37-42.
- 825 Millard, A., 2006a. Bayesian analysis of ESR dates, with application to border cave. *Quaternary*
826 *Geochronology* 1, 159-166.
- 827 Millard, A., 2006b. Bayesian analysis of Pleistocene chronometric methods. *Archaeometry* 48, 359-
828 375.
- 829 Murray, A. S., Wintle, A. G., 2000. Luminescence dating of quartz using an improved single-aliquot
830 regenerative-dose protocol. *Radiation Measurements* 32, 57-73.
- 831 Murray, A.S., Olley, J.M., 2002. Precision and Accuracy in the Optically Stimulated Luminescence Dating
832 of Sedimentary Quartz: A Status Review. *Geochronometria* 21, 1-16.
- 833 Murray, A. S., Wintle, A. G., 2003. The single aliquot regenerative dose protocol: potential for
834 improvements in reliability. *Radiation Measurements* 37, 377-381.
- 835 Murray, A.S., Buylaert, J.-P., Thiel, C., 2015. A luminescence dating intercomparison based on a Danish
836 Beach-ridge sand. *Radiation Measurements* 81, 32-38.
- 837 Nathan R.P, Mauz B., 2008. On the dose-rate estimate of carbonate-rich sediments for trapped charge
838 dating. *Radiation Measurements* 43, 14-25.
- 839 Nelson, M. S., Rittenour, T. M., 2015. Using grain-size characteristics to model soil water content:
840 Application to dose-rate calculation for luminescence dating. *Radiation Measurements* 81, 142-149.
- 841 Philippe, A., Guérin, G., Kreutzer, S., 2019. "BayLum" an R package for Bayesian Analysis of OSL Ages
842 & Chronological Modelling. *Quaternary Geochronology* 49, 16-24.
- 843 Philippe, A., Vibet, M., 2020. "Analysis of Archaeological Phases Using the R Package ArchaeoPhases.
844 *Journal of Statistical Software, Code Snippets*, 93(1), 1–25.
- 845 Prescott, J.R., Hutton, J.T., 1988. Cosmic ray and gamma ray dosimetry for TL and ESR. *Nuclear Tracks*
846 *and Radiation Measurements*, 14, 223-227.
- 847 R Core Team, 2020. R: A Language and Environment for Statistical Computing. R Foundation for
848 Statistical Computing, Vienna, Austria. <https://r-project.org>



- 849 Reimer, P. J., Austin, W. E., Bard, E., Bayliss, A., Blackwell, P. G., Ramsey, C. B., ... & Grootes, P. M.
850 (2020). The IntCal20 northern hemisphere radiocarbon age calibration curve (0–55 cal
851 kBP). *Radiocarbon*, 62(4), 725–757.
- 852 Richter, D., Dombrowski, H., Neumaier, S., Guibert, P., Zink, A., 2010. Environmental gamma dosimetry
853 for in-situ sediment measurements by OSL of α -Al₂O₃:C. *Radiation Protection Dosimetry* 141, 27–35.
- 854 Thomsen, K.J., Murray, A.S., Bøtter-Jensen, L., 2005. Sources of variability in OSL dose measurements
855 using single grains of quartz. *Radiation Measurements*, 39, 47–61.
- 856 Thomsen, K.J., Murray, A.S., Buylaert, J.-P., Jain, M., Helt-Hansen, J., Aubry, T., 2016. Testing single-
857 grain quartz OSL methods using known age samples from the Bordes-Fitte rockshelter (Roches d'Abilly
858 site, Central France). *Quaternary Geochronology* 31, 77–96.
- 859 Tribolo, C., Mercier, N., Valladas, H., 2001. Alpha sensitivity determination in quartzite using an OSL
860 single aliquot procedure. *Ancient TL* 19, 47–50.
- 861 Wintle, A.G., Murray, A.S., 2006. A review of quartz optical stimulated luminescence characteristics
862 and their relevance in single-aliquot regeneration dating protocols. *Radiation Measurements*, 41, 369–
863 391.
- 864 Zimmerman, D.W., 1971. Thermoluminescence dating using fine grains from pottery, *Archaeometry*
865 13, pp. 29–52.
- 866



867 **Figures**

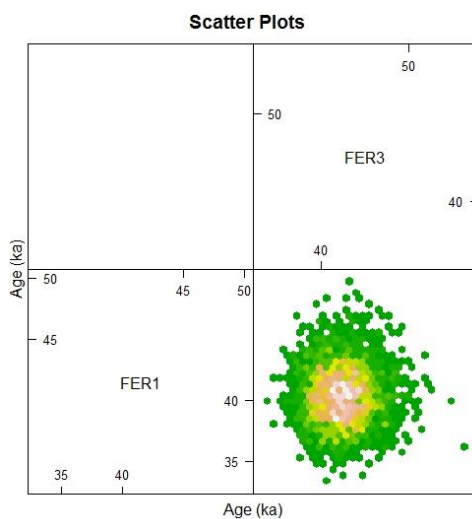


868

869 **Fig. 1:** Age estimates for OSL samples FER 1 and FER 3. The red circles indicate the Bayes estimates of
870 the age (*i.e.* the most likely values) for each sample; the cyan and blue bars represent the 68% and
871 95% credible intervals, respectively. For the two radiocarbon ages (C14-1 and C14-2), the reader is
872 referred to section 6.

873

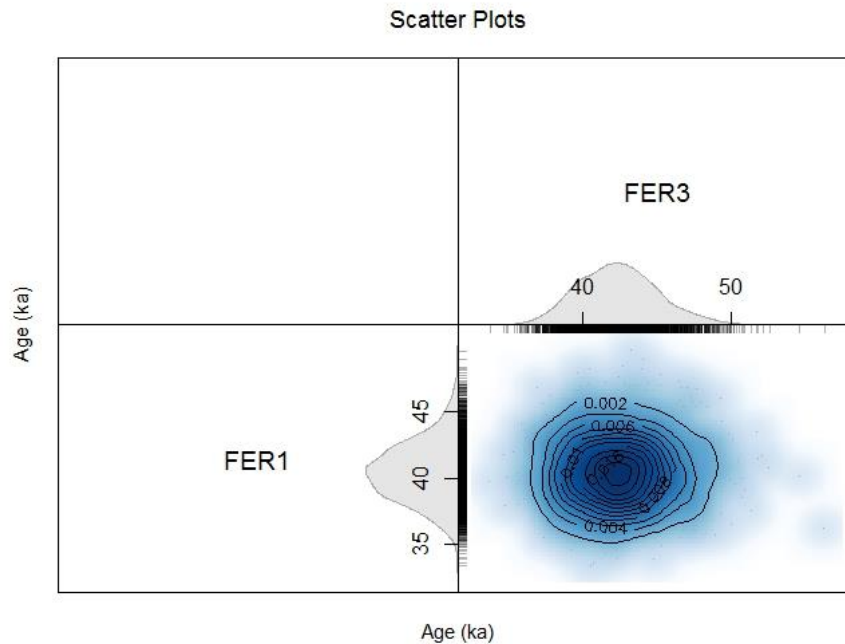
874



875

876 **Fig. 2:** Bivariate scatter plot as hexagon plot presentation of a sample of observations from the joint
877 posterior distribution of the two OSL ages considered independently (no stratigraphic constraints, no
878 off-diagonal members in the covariance matrix). In such a plot, each point corresponds to one
879 realisation of the ages of the two samples generated by the MCMC. Note: the reason for having this
880 figure in the cell of an array is not visible here; it becomes useful when calculating ages for more than
881 2 samples, in which case for each pair of samples, a similar plot appears in the appropriate cell.

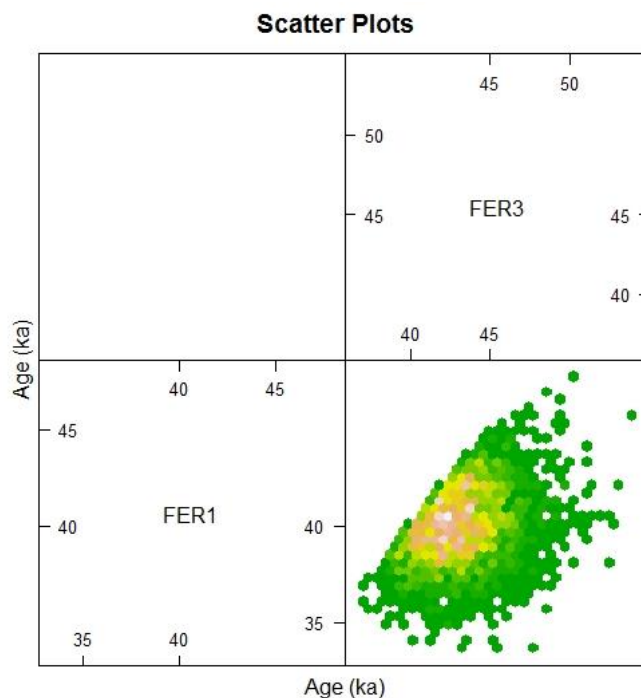
882



883

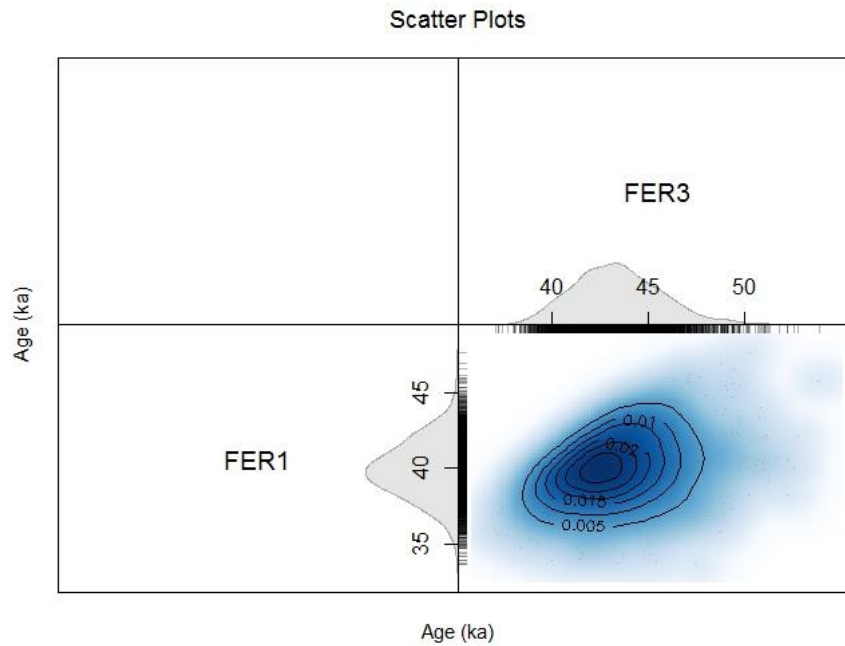
884 **Fig. 3:** Probability densities for the OSL ages estimated jointly with the same model as that used to
885 generate Fig. 2, based on Kernel Density Estimates (KDE), and marginal probability densities. The bell-
886 shape and symmetry of the scatter plot indicate the absence of correlation between the two ages.

887



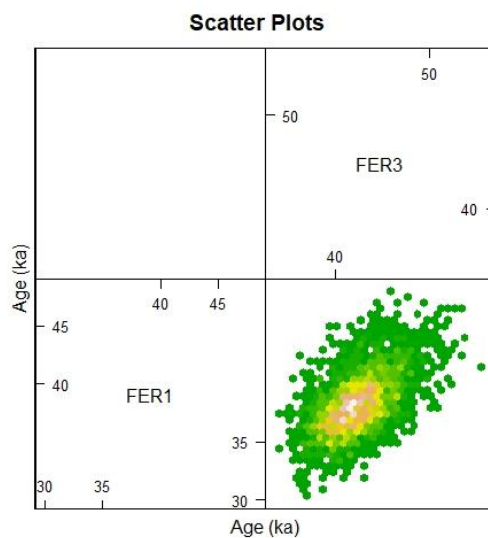
888
889 **Fig. 4:** Bivariate scatter plot from the joint posterior distribution of the ages of samples FER 1 and FER
890 3 when a stratigraphic constraint is applied (sample FER 1 is younger than sample FER 3) but with no
891 off-diagonal members in the covariance matrix. The truncation in the upper-left hand corner scatter
892 plot indicates the effect of the stratigraphic constraint.

893

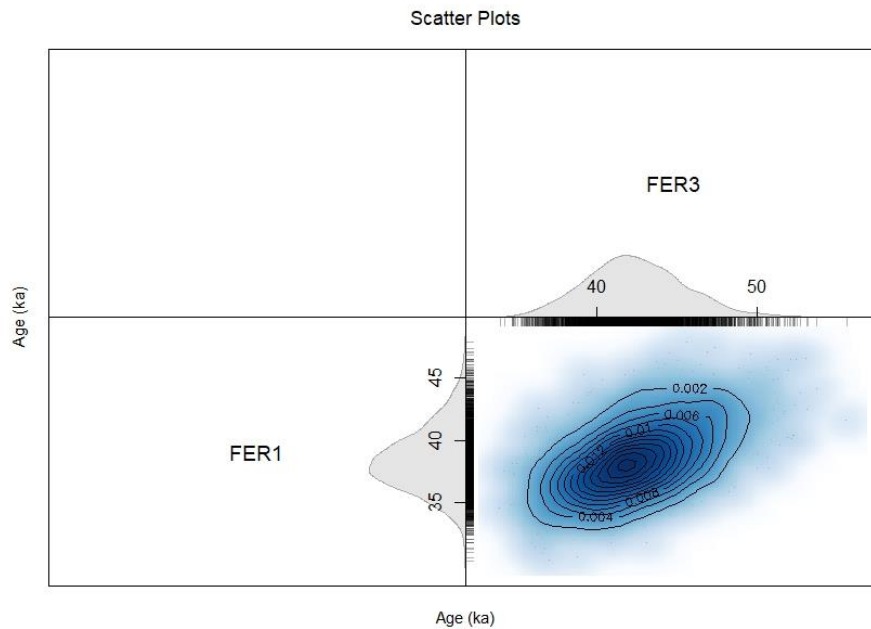


894
895 **Fig. 5:** Probability densities for the OSL ages estimated jointly, using the same model as that
896 implemented to generate Fig. 4 (stratigraphic constraint, no covariance matrix).

897



898
899 **Fig. 6:** Bivariate scatter plot from the joint posterior distribution of the ages of samples FER 1 and FER
900 3 when a stratigraphic constraint is applied (sample FER 1 is younger than sample FER 3) and off-
901 diagonal members of covariance matrix are used to model systematic errors (note: in this case, for
902 illustrative purposes we used a simplistic covariance matrix – see section 5.3.1. for details). The
903 truncation in the upper-left hand corner scatter plot indicates the effect of the stratigraphic constraint.
904



905
906 **Fig. 7:** Probability densities for the OSL ages estimated jointly, using the same model as that
907 implemented to generate Fig. 6 (stratigraphic constraint and off-diagonal members in the covariance
908 matrix). The positive correlation in the joint posterior density reflects the effect of modelling the
909 systematic errors with a covariance matrix (and, to some degree, of the stratigraphic constraint).
910



911 **Table 1.** Summary of Credible Intervals for the ages (in ka) of samples FER 1 and FER 3 estimated in
 912 the different modelled scenarios.

Sample	68% Confidence Interval		95% Confidence Interval	
	lower	upper	lower	upper
Independent				
FER 1	36.0	40.5	34.1	43.3
FER 3	38.9	44.6	36.6	47.8
In stratigraphy				
FER 1	36.2	40.4	34.3	42.9
FER 3	40.0	45.0	38.1	48.5
No stratigraphic constraint, with 'simplistic' covariance (section 5.3.1)				
FER 1	36.0	40.8	33.9	43.8
FER 3	39.2	45.4	36.7	48.1
In stratigraphy, with realistic covariance (section 5.3.2)				
FER 1	36.1	40.5	34.2	42.6
FER 3	39.8	45.3	37.8	48.6
In stratigraphy, with covariance and a 'young' radiocarbon age				
FER 1	35.2	39.4	33.3	41.2
FER 3	39.2	42.2	36.9	42.3
In stratigraphy, with covariance and an 'old' radiocarbon age				
FER 1	38.7	43.5	36.2	46.2
FER 3	46.1	48.7	46.1	51.5

913

914



915 **Table 2.** List of physical units and associated uncertainties used in this work. The letter i in subscript
 916 indicates a sample specific value, its absence a common value shared between samples. The letter s
 917 indicates absolute uncertainties, while σ is used for relative uncertainties.

Physical unit	Notation	Systematic uncertainty	Random uncertainty
Laboratory source dose rate	\dot{d}_{lab}	σ_{lab}	
Cosmic dose rate	$\dot{d}_{cosmic,i}$		$s_{cosmic,i}$
K concentration	$[K]_i$	σ_K	$\sigma_{K,i}$
U concentration	$[U]_i$	σ_U	$\sigma_{U,i}$
Th concentration	$[Th]_i$	σ_{Th}	$\sigma_{Th,i}$
Internal dose rate	\dot{d}_{int}	s_{int}	
Gamma dose rate	$\dot{d}_{\gamma,i}$	σ_{γ}	$\sigma_{\gamma,i}$
Water content	WF_i		$s_{WF,i}$

918